PNAS RESEARCH ARTICLE | PHYSICS OPEN ACCESS

Statistical signature of electrobreakdown in graphene nanojunctions

Charalambos Evangeli[a,1,2], Sumit Tewari[a,1,2], Jonathan Marcell Kruip[b], Xinya Bian[a], Jacob L. Swett[a], John Cully[a], James Thomas[a], G. Andrew D. Briggs[a], and Jan A. Mol[b]

Edited by Risto Nieminen, Aalto-Yliopisto Teknillisen Fysiikan Laitos, Espoo, Finland; received October 17, 2021; accepted March 28, 2022

Controlled electrobreakdown of graphene is important for the fabrication of stable nanometer-size tunnel gaps, large-scale graphene quantum dots, and nanoscale resistive switches, etc. However, owing to the complex thermal, electronic, and electrochemical processes at the nanoscale that dictate the rupture of graphene, it is difficult to generate conclusions from individual devices. We describe here a way to explore the statistical signature of the graphene electrobreakdown process. Such analysis tells us that feedback-controlled electrobreakdown of graphene in the air first shows signs of joule heating-induced cleaning followed by rupturing of the graphene lattice that is manifested by the lowering of its conductance. We show that when the conductance of the graphene becomes smaller than around 0.1 G_0, the effective graphene notch width starts to decrease exponentially slower with time. Further, we show how this signature gets modified as we change the environment and or the substrate. Using statistical analysis, we show that the electrobreakdown under a high vacuum could lead to substrate modification and resistive-switching behavior, without the application of any electroforming voltage. This is attributed to the formation of a semiconducting filament that makes a Schottky barrier with the graphene. We also provide here the statistically extracted Schottky barrier threshold voltages for various substrate studies. Such analysis not only gives a better understanding of the electrobreakdown of graphene but also can serve as a tool in the future for single-molecule diagnostics.

graphene | electrobreakdown | statistics | resistive switching | vacuum

Significance

We present here the statistical signature of the joule heating of graphene nanojunctions up to its rupture limit. Our results over different substrates help us derive conclusions that are rather difficult to make and comprehend by studying complex individual IV traces of electrobreakdown of graphene in air and vacuum environments. These statistically robust conclusions can find their application in making quantum dots, resistive switches, and well-defined single-molecule junctions and even in rupture analysis of graphene interconnects in future complementary metal-oxide semiconductor (CMOS) devices.

Whether it is the confirmation of molecular reality by French physicist Jean Perrin (1) in 1909 or the famous 1916 article "The Atom and the Molecule" by Gilbert Lewis (2) to name a few, the dawn of the 20th century demonstrated immense interest and advancement in our understanding of the fundamental constituents of matter. It was only in the latter half when, with the work of Aviram and Ratner (3), researchers started to discuss how to use single molecules and atoms as electronic devices. With the invention of the scanning tunnelling microscope (STM) (4, 5) in 1981, it became possible to see and contact single molecules and atoms (6, 7). Soon after in 1992, Muller et al. (8) developed the mechanically controlled break junction (MCBJ) technique and and in 1993 Agraït et al. (9) developed the STM break junction (STM-BJ), which can be used to controllably create atomic-scale point contacts and tunnel junctions. The simplicity of both the techniques made them immensely popular in the molecular electronics community. In MCBJ, a metallic notched wire is controllably pulled apart using piezo motors and the current through the junction is recorded. Similarly, in STM-BJ the tip is moved vertically, in and out of contact with the substrate to form and break metallic contacts. Later, Krans et al. (10) inferred by constructing histograms from the junction conductance values during the rupture of Cu and Al that right before the junction breaks down into tunnelling a single-atom contact is formed. Later a similar conductance quantization was also shown for Au junctions (11–13). These conductance histograms became the workhorse for studying electron transport through single molecules (14). The main benefit of using such statistical analysis over studying individual traces is that it allows averaging over many different atomic configurations to find the most stable of them.

In the last decade, researchers in the field of molecular electronics have explored extensively the use of graphene as electrodes to bind and study single molecules (15–17). These electrodes are more stable than metallic electrodes even at room temperature, due to the reduced mobility of carbon atoms connected with sp^2 carbon bonds. Graphene's two-dimensional structure also allows a reduction in the screening of the gate potential compared to the metallic electrodes and produces negligible image charge effects. A controlled joule heating or electrobreakdown (EB) is used to break graphene in a controlled manner and create electrodes separated by nanometer-sized tunnel gaps. This process is also called electroburning when oxygen is present in the environment; however,

Author affiliations: [a]Department of Materials, University of Oxford, Oxford OX1 3PH, United Kingdom; and [b]School of Physics and Astronomy, Queen Mary University of London, London E1 4NS, United Kingdom

Author contributions: C.E., S.T., J.T., G.A.D.B., and J.A.M. designed research; C.E., S.T., J.M.K., J.L.S., and J.C. performed research; X.B., J.C., and J.T. contributed new reagents/analytic tools; C.E., S.T., and J.A.M. analyzed data; and C.E., S.T., and J.A.M. wrote the paper.

The authors declare no competing interest.

This article is a PNAS Direct Submission.

[1]C.E. and S.T. contributed equally to this work.

[2]To whom correspondence may be addressed. Email: mecsumit@gmail.com or ch.evangeli@gmail.com.

This article contains supporting information online at https://www.pnas.org/lookup/suppl/doi:10.1073/pnas.2119015119/-/DCSupplemental.

Published June 27, 2022.

as we further discuss, it fails to describe the breakdown process in vacuum. Both EB and BJ techniques can result in tunnel junctions with unknown atomic configuration that affects the electronic transport characteristics of the leads and also the single-molecule junctions measured with these electrodes (14). Current has been also used for cleaning of graphene (18) and for sculpting of edges in graphene (19). In BJs, the junction formation is a purely mechanical outcome due to the pulling action on the two ends of a notched wire (with the exception of the electromigrated break junction) and thus can be modeled using pure molecular dynamic simulations (20–22). On the contrary, the EB process used to make graphene junctions has complex electron–atom interactions in play and cannot be modeled by molecular dynamics. Recently, we have shown that the start of the electrobreakdown process can be modeled sufficiently accurately using electron–phonon interactions (23). It is very difficult, however, to model the whole process amid many dependent factors that can influence it, such as the substrate, the environment, the quality of the graphene, starting configuration, localized thickness variation, localized charge accumulations, new defects formation, and more. The characterization of the width of the nanogap formed by EB is also difficult using direct measurement methods (like scanning electron microscopy [SEM]/transmission electron microscopy [TEM]/scanning tunnelling microscopy [STM]/atomic force microscopy [AFM]) and is commonly estimated by fitting the IV characteristics (or resistance) using the Simmons model. The Simmons model has been derived for three-dimensional (3D) metallic electrodes (24) (along with a recent erratum) (25) and its use has not been verified for two-dimensional (2D) electrodes. Currently, for graphene electrodes, it is used with a few free parameters: the gap width, the barrier height, the cross-section area of the junction, and the asymmetry in the bias voltage response. Among others, the cross-section area of the junction is difficult to estimate, as there is no reason to assume the cut made by EB forms two parallel edges on the electrodes. Thus this value has to be fixed manually. Approximate values for the barrier height reported by different groups are around 0.24 to 0.5 eV, which are much smaller than the work function of graphite (around 5 eV) (17). Moreover, substrate effects (if any) on the tunnelling process could lead to a broad range of possible values for the barrier height. Thus one should be leery of the gap width obtained by the Simmons model for graphene electrodes.

Most of the experimental demonstrations for visualizing EB or joule heating of graphene using TEM/SEM are performed on suspended graphene devices (26–28) or on top of thin membranes (29). However, for large-scale fabrication of graphene quantum dots and stable nanometer gaps, the EB has to be performed on a substrate and thus it is very important to understand it in this configuration. Candini et al. (30) have shown that graphene on SiC electroburns normally under ambient conditions, but it does not break at all under vacuum. On comparing this to electrobreakdown on a SiO_2 substrate Candini et al. (30) claim that the substrate's oxygen content plays a role in vacuum electrobreakdown (VEB). On the contrary, El Abbassi et al. (31) claim that the substrate plays no role in VEB. They used a pulsed electrobreakdown technique where instead of slow controlled saw-tooth pulses, sharp square pulses of varying heights were used. Additionally, they report that at higher fields (bias $\approx$ 9 V) electroforming of the SiO_2 substrate can occur (32), giving rise to switching behavior; however, they did not see any switching behavior on silicon nitride substrates, thus claiming that it is a substrate-dependent phenomenon. Electroforming is an electrical breakdown process usually reported in metal–insulator–metal junctions. However, it is not an irreversible breakdown, but is instead followed by resistive switching of the newly formed conducting pathways in the insulator. There is a simple way to not confuse between electrobreakdown and electroforming. Electrobreakdown is a term used to represent joule heating of graphene from nanometer-size junctions to breakdown. Electroforming in graphene occurs at the end of the electrobreakdown process, when a small tunnel gap is opened between the two newly formed graphene electrodes. The electroforming voltage depends on the size of the gap between the electrodes (33) and usually is above 20 V. Nevertheless, Chang et al. (34) have shown that vertically stacked SiO_2 60-nm thin films can be electroformed at 8 V. He et al. (35, 36) studied electroforming and resistive switching in a graphene–SiO_2 –graphene structure under vacuum (Table 1). The graphene is ruptured here via joule heating (without feedback) and the voltage is increased (even after graphene breakdown) to a forming voltage (10 V) that initiated resistive switching. The gap between the two graphene electrodes in their case is around 30 to 100 nm. This gives rise to ON and OFF resistive states with set and reset voltages of around 2.8 and 5.5 V, respectively. They have shown via high-resolution TEM images that these resistive states are formed due to a channel of crystalline Si nanoparticles created between the two graphene electrodes. Such a switching is not observed when the rupture is performed under ambient conditions, where the reduction of SiO_2 to Si nanoparticles is not feasible. Usui et al. (37) laid down three mechanisms according to which the electrical breakdown of SiO_2 thin films can take place—impact ionization, trap creation, and anode hole injection. They show that SiO_2 films smaller than 10 nm remain stable below 2.7 V/nm field strength and that above this electrical breakdown takes place. Resistive switching behavior is also observed in suspended graphene devices (i.e., without any substrate effect) (27) with a comparable switching ON (2.5 to 4.5 V) and OFF (8 V) pulse.

The exact mechanism of EB in different environments (air or vacuum) has been debated previously and a primary consensus is that the EB in air happens due to oxidation while in vacuum it happens due to sublimation. However, there is no consensus on the effect of the environment and the substrate. Unlike BJ, the EB process has not been explored so far by performing detailed statistical analysis. The underlying reason is that in BJ, continuous rupture-formation steps can be performed, giving large statistical sets, which is not feasible in the EB process.

Table 1. Resistive switching: Comparison of various switching parameters derived in our study with others found in the literature

Ref.	MIM	Process	Tunnel gap, nm	$V_{forming}$, V	V_{set}, V	V_{reset}, V
He et al. (35)	Gr-SiO_2-Gr	Joule heating	>30	10	2.8	5.5
Chang et al. (34)	TaN-SiO_2-Si	Lithography	60	8	3.5	4
Posa et al. (32)	Gr-SiO_2-Gr	Joule heating	<5	9	4.4	5.5
Our work	Gr-SiO_2-Gr	Joule heating	—	<5	2.3	4
	Gr-Al_2O_3-Gr	Joule heating	—	<5	2.8	5
	Gr-AlN-Gr	Joule heating	—	<5	2.3	4.8

MIM, metal–insulator–metal.

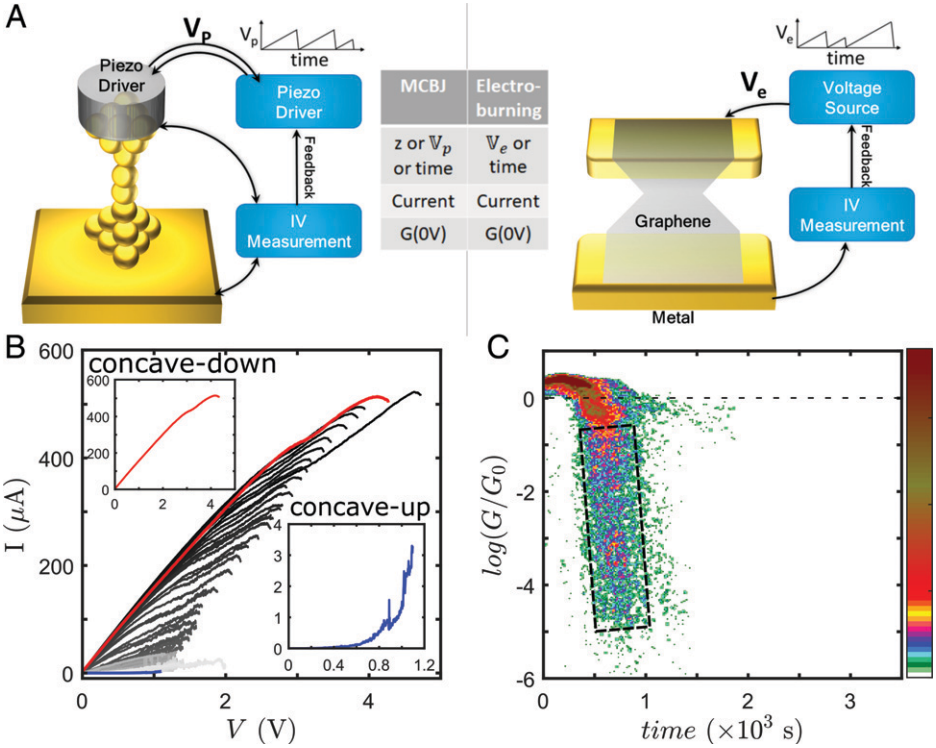

Fig. 1. (*A*) Schematic comparison of BJ and electrobreakdown. In MCBJ, a notched metal (M) wire is broken with the help of a piezo that is powered by sawtooth-shaped voltage ramps [$V_p(t)$]. These ramps are feedback controlled by the current values measured across the junction. This is similar to electrobreakdown where a graphene nanoconstriction (Gr) is burned using a feedback-controlled sawtooth-shaped voltage ramp [$V_e(t)$]. The table provides analogous terms between the two methods. (*B*) Typical IV trace fan plot of EB process in ambient conditions. (*Inset*) Examples of concave-up and concave-down IV traces. (*C*) Two-dimensional zero bias conductance histogram for electrobreakdown of graphene on SiO_2 under ambient conditions of 132 devices.

In this article we show a way to map the statistical signature of electrobreakdown in graphene nanojunctions by analyzing lots of data for hundreds of devices and use this to study the effects of different environments and substrates. Such an analysis helps to make conclusions that would be rather difficult to make and comprehend by studying individual traces that are collected during the complex set of events that happen while in electrobreakdown. Performing a statistical analysis also takes care of the device-to-device variations.

Statistical Analysis

To understand how, in the absence of continuous rupture–formation steps, a statistical analysis of electroburned junctions can be performed, we have to first look closely into how the EB process takes place. EB corresponds to the rupture of the carbon lattice of graphene by passing a large electrical current through it. In 2011, Prins et al. (15) devised a procedure to perform EB in a feedback-controlled manner that has been widely used since then. In this paper, first a narrow constriction (a few hundred nanometers wide) is formed in graphene using a standard electron-beam lithography technique. A steadily increasing voltage ramp (around 5 V/s) is then applied over this graphene nanoconstriction using prefabricated contact pads while continuously monitoring the current. A feedback loop is switched on if a sudden decrease in the current of more than 5% is recorded. Once the feedback loop is initiated, the voltage is quickly ramped down to zero with a rate of around 500 V/s. The sudden decrease in current is seen as a sign of the rupture of carbon–carbon bonds close to the nanoconstriction and thereby a reduction in the constriction's width. The cycle is then repeated until the constriction breaks down completely and a tunnel junction is formed.

Two-Dimensional–Conductance Histogram

The EB process has a close procedural analogy with BJ, which forms the basis of our statistical analysis. Two-dimensional histograms of normalized conductance on the vertical axis and net z distance traveled by the piezo in the horizontal axis have been drawn earlier for analyzing MCBJ experiments (38). They proved to be useful in detecting multiple stable configurations and to obtain a size measurement of a molecular bridge, if any. In BJ, the (metallic) junction is formed and broken in repeated piezo cycles driven by sawtooth voltage pulses ($V_p(t)$) swept at a constant rate (Fig. 1*A*). Thus, the net z distance swept by the piezo is proportional to the net accumulated voltage ($\mathbb{V}_p$) or the time (t). Even though the current (I) is continuously recorded in these experiments, the conductance values plotted in the 2D histogram are usually collected at the end of each piezo sweep [$G(0V)$]. This is done to avoid the effect of cross-talk between the piezo high-voltage line and the current measurement line.

For EB of the graphene we also utilize a similar feedback-controlled sawtooth voltage pulse [$V_e(t)$], which is swept at a fixed rate ($r = 5$ V/s); see Fig. 1*B* for a typical fan plot for the IV traces during EB. Thus, in analogy with the BJ, one can construct a 2D histogram with the vertical axis as conductance (in the units of conductance quantum, G_0), measured at the start of each voltage sweep (thus a zero-bias conductance), while the horizontal axis is forward accumulated voltage ($\mathbb{V}_e$) or time ($\mathbb{V}_e$/r). The EB finishes when the junction is broken to a threshold resistance (around 1 Gohm) or a maximum of 200 cycles. Fig. 1*C* shows such a 2D-conductance histogram of electrobreakdown of graphene on SiO_2 substrate in air. The histogram counts are calculated by binning linearly the time data and logarithmically the normalized conductance data and the counts are represented by a color bar. This can be seen as a signature plot of EB of

graphene on SiO_2 in air. We have chosen a colormap with discrete colors to show all the data at a complete range and to be able to show all features in the different plots with the same colormap. This kind of colormap is typically used in 2D histograms of BJ experiments (39) (see also *SI Appendix* for a comparison between linear and nonlinear colormaps).

Before we discuss how this signature 2D-histogram plot modifies as we change the substrate and/or the environment, let us point out some marked differences between this and standard 2D-conductance histograms plotted for metallic junctions. In metallic junctions formed using the BJ technique the 2D histograms usually show a sudden drop once the junction is broken. After this, an exponential drop in conductance signifies the tunnelling regime. The sudden drop is usually attributed to the pullback effect or jump out of contact where after the junction is broken the apex atoms in the two newly formed freely suspended electrodes relax. This relaxation happens at picosecond timescales, producing a sudden drop in conductance. Such a sudden jump is not visible in the case of the graphene EB owing to the stable hexagonal lattice structure of graphene and the van der Waals interaction between graphene and the substrate (40).

We see, however, a region where the conductance drops exponentially with time (Fig. 1*C*). Fitting suggests that the normalized conductance (G/G_0) drops an order of magnitude roughly every 43 s. Han et al. (41) and Qi et al. (42) have shown experimentally that the intrinsic conductance of graphene varies linearly with the width of the notch; i.e., $G = 0.15\frac{e^2}{h}w$. This linear dependence of conductance on the width, in combination with the exponential decrease of conductance with time that we have found in our statistical analysis, suggests that the effective width of the notch decreases exponentially slower with time during the end part of the EB process (enclosed with dashed black lines in Fig. 1*C*). Considering the complexity of a joule-heating–induced breakdown of graphene lattice, it would be naive to assume that the breakdown happens edge to edge. Rather, there could also be initiation points in the bulk of the graphene where the carbon lattice might break and/or localized increase of disorder can happen. This can cause formation of multiple potential barriers and scattering centers. Thus it would be more appropriate to talk in terms of effective notch width. The exponentially slower decrease of effective notch width could be attributed to the decrease of the current that passes through the device as the defects in the vicinity of the notch increase. There is, however, also a role that the feedback loop plays here, which we discuss in the next section.

At the start of the EB, the 2D-conductance histogram shows that there is a rise in the conductance of the graphene nanojunction. This is due to the current-induced cleaning of the graphene, which initially improves the transport through the graphene. After that when the carbon lattice starts to rupture, more and more defects are formed near the constriction and the effective notch width decreases and thus the conductance starts to drop. As we have discussed in our recent publication (23), in vacuum conditions, the transport through the graphene remains diffusive until the zero-bias conductance is above 1 G_0. In this regime, the current increases linearly and then starts to saturate at high electric fields. This has been attributed to the activation of optical phonons (23).

Effect of the Environment in the Conductance Histogram

We have shown so far the statistical signature of electrobreakdown of graphene on SiO_2 in the air. In Fig. 2 we show 2D-conductance histogram plots of electrobreakdown in vacuum. We observe

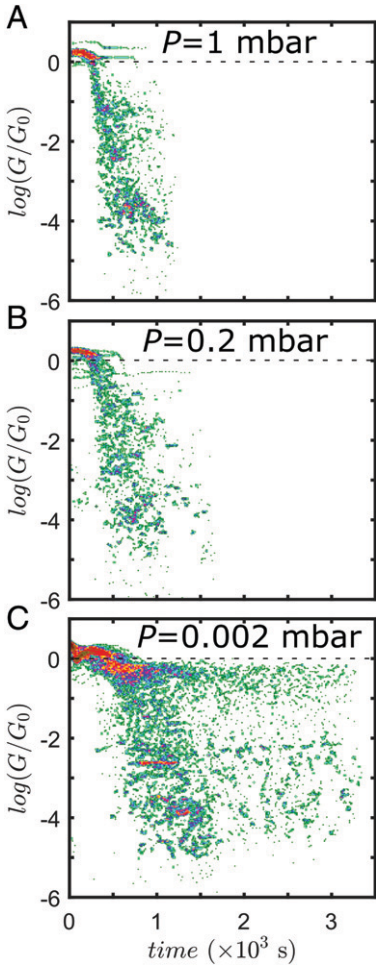

Fig. 2. (*A–C*) Change in the statistical signature of the electrobreakdown process for graphene on a SiO_2 substrate for different pressures: (*A*) $P = 1$ mbar for 31 devices, (*B*) $P = 0.2$ mbar for 38 devices, and (*C*) $P = 0.002$ mbar for 95 devices.

here that just by changing the environment the 2D-conductance histogram shows a completely different signature while everything else is kept the same, including the shape and the rate of the voltage ramps, the feedback condition, the substrate, and the initial notch size. The three plots Fig. 2 *A–C* show how the histogram signature changes while lowering the vacuum chamber's pressure. Two important features to note here in the high-vacuum data are the following: First, the burning takes a much longer time and many junctions here never progress to a conductance value below the threshold setpoint and the process has to be aborted after 200 cycles. Second, the histogram does not show a clear exponential drop of conductance with time as we observed in air; rather, a horizontal band appears slightly below 1 G_0.

To deepen our understanding we built a conductance-curvature histogram. Here, the individual traces are further classified into two categories depending on the curvature of the IV plots during each trace—a concave-down ($\frac{d^2I}{dV^2} \leq 0$) and a concave-up ($\frac{d^2I}{dV^2} > 0$) curvature, as shown in Fig. 1 *B*, *Insets*. We then rank the individual traces based on the strength of their curvature (in both positive and negative directions). For this, we did an empirical fit of individual traces to a quadratic polynomial ($I = aV^2 + bV + c$) and the coefficient (a) of the quadratic term provided the required values. Using this we plot a conductance-curvature histogram shown in Fig. 3*B*. To construct this, 95 high-vacuum electrobroken devices were used. For comparison, we also plot a

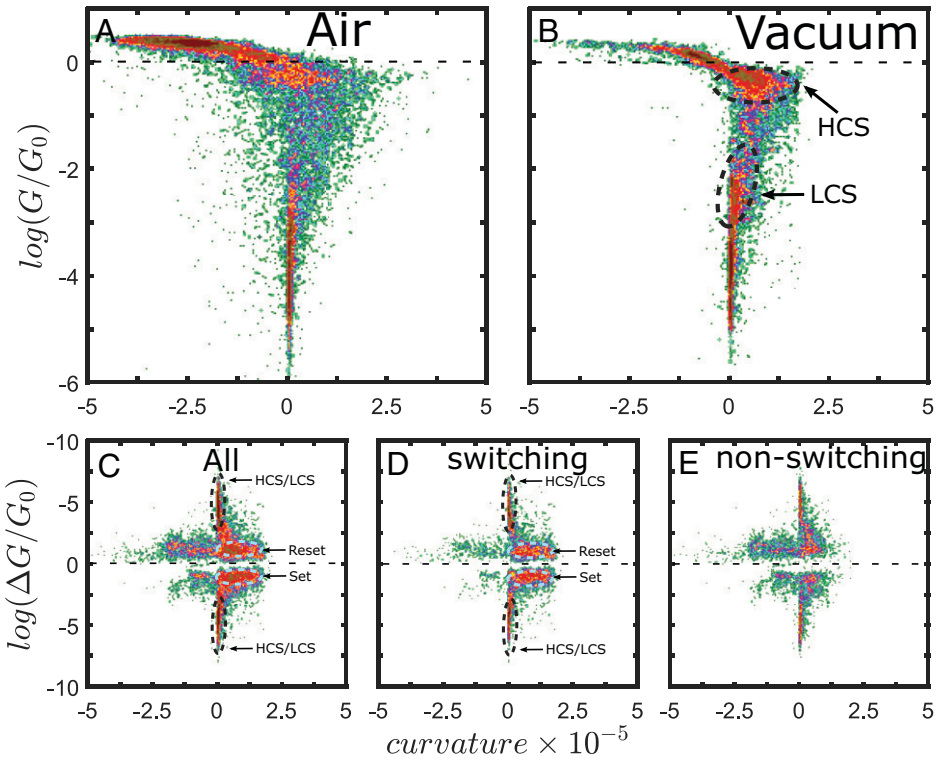

Fig. 3. Two-dimensional conductance-curvature histogram for electrobreakdown under (*A*) ambient conditions for 132 devices and (*B*) vacuum for 95 devices (same as in Fig. 2*C*). The thick black dashed ovals encircle the LCS and HCS. (*C*) $\frac{\Delta G}{G_0}$ histogram constructed with all the vacuum datasets. Here, $\Delta G = G[i] - G[i-1]$ and $G[i]$ is the zero-bias conductance at the end of the ith cycle. ΔG is negative for reset processes and positive for set processes of the resistive switching behavior and they are enclosed in light-blue dashed ovals.

similar histogram for EB in air (Fig. 3*A*). The positive curvature corresponds to tunnelling (exponential) IV characteristics and so at low conductance values we see statistically more counts on the positive side of the curvature. This is visible both in the VEB and the atmospheric electrobreakdown. Similarly at the start of the EB when the conductance values are high, we are in a diffusive regime as mentioned earlier and so we expect to see statistically more counts on the negative side of the curvature axis. However, in the VEB case, the conductance curvature histogram shows that there is an accumulation of points appearing on the positive curvature side at high conductance values, slightly below 1 G_0. Earlier we noticed that such a localization in the 2D-conductance histogram occurs only along the conductance axis and was spread around the time axis; however, we see now that it is localized also around a specific curvature value. A similar localization is also noted in the power-curvature histogram in *SI Appendix*, Fig. S1. Here, power was calculated from the maximum current and voltage value for each EB cycle. These two separate localized groups correspond to a low-conductance state (LCS) and a high-conductance state (HCS) and point toward a switching behavior. We confirmed this also by checking individual traces. Fig. 4*A* shows an individual switching device during VEB using a normalized zero-bias conductance variation plot with an EB cycle index. Resistive switching is initiated after around cycle index 40 in this example and then the device starts switching between two conductance states. Thirty-one of 95 devices studied show this behavior. These along with all the other devices constitute the HCS and LCS regions marked in Fig. 3*B*. The IV forward (purple arrow) and return (pink arrow) traces together selected at the yellow and red points in Fig. 4*A* show the set and reset actions (Fig. 4 *B* and *C*). A resistive switching between a LCS and a HCS points toward some type of electroforming process happening. For electroforming, the voltage across the dielectric has to be ramped up until an electroforming voltage is reached and the resistive switching is activated. This voltage depends on the width of the dielectric or the gap between the electrodes. The smaller the gap is, the smaller the electroforming voltage. Nevertheless, it has been shown that resistive switching can also be initiated without electroforming (43–45). In the feedback-controlled EB protocol that we use, a predetermined forming voltage was not applied. We do not know whether we are tapping into an electroforming-free (or self-electroformed) resistive switching behavior here, but we can extract an upper limit to the forming voltage, if any, that we might have reached during EB of the graphene. This will be the maximum voltage just before the resistive switching is initiated. For the complete vacuum dataset, the mean set and reset voltages are 2.5 and 4 V, respectively, and the upper limit of the extracted electroforming came out to be equal to the mean reset voltage. Fig. 4*D* has two one-dimensional (1D) histograms showing the distribution of set and reset voltages extracted from all the switching points (for example, the yellow and red points in Fig. 4*A*) in all the devices.

Discussion on the Effect of Feedback

The electrobreakdown described in this article is performed using a usual feedback-controlled procedure (16). This feedback plays a role in the statistical signatures shown earlier and should be addressed. In Fig. 1*C* we show that the graphene junction gets initially cleaned using joule heating with an increase in conductance followed by a decrease, which signifies the start of the rupture of graphene lattice, which becomes exponentially slower at the end. Some of these features should be there even if the burning is done without feedback; however, the whole process will then go much faster. The feedback slows down the process leading to controlled electrobreakdown and pronouncing certain features in the histogram, which is explained below. The same happens with

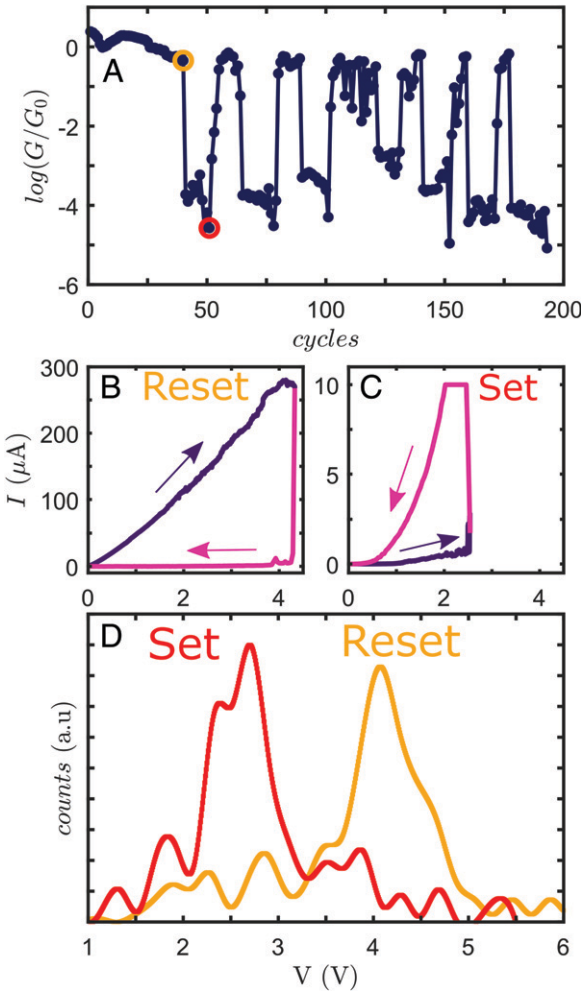

Fig. 4. (*A*) An example device showing evolution of individual zero-bias conductance over all the cycles showing the switching behavior observed statistically in Fig. 3. The yellow and red circles show the first pair of set and reset points in the device. (*B* and *C*) Individual examples of a reset and set where zero-bias conductance cycles from HCS to LCS (*B*) and from LCS to HCS (*C*). (*D*) Joint 1D histograms showing the distribution of set and reset voltages, constructed using devices showing switching behavior for SiO_2 substrate (31 of 95).

the VEB and especially the switching behavior. We have shown how VEB leads to resistive switching behavior. As shown by He et al. (35, 36), in SiO_2 this switching behavior is a result of the formation and reoxidation of crystalline Si-nanoparticles (cSiNP) arrays. The feedback control again slows down this oxidation reduction process. For example, if the system is in the HCS, this means there is a more dense network of these cSiNP between the two graphene electrodes. If we ramp up the voltage across electrodes with the feedback ON, the feedback gets triggered at small electrostatic rearrangements of the cSiNP and ramps the voltage back to zero. This will lead to multiple points that we see in the HCS plateaus (Fig. 4*A*). The HCS plateaus end when a reset voltage is reached, causing oxidation of many of the cSiNP to SiO_2, and the system moves to the LCS. A similar effect of feedback triggering would also lead to the points in the LCS plateaus. Together these extra points in the HCS and LCS plateaus give rise to more counts seen in the HCS and LCS regions in Fig. 3 *E* and *G* even though only around one-third of the devices were showing switching behavior. Recently, Pósa et al. (46) showed that the resistance noise of the junction could also trigger false feedback events.

As we mentioned, the feedback parameters affect the HCS and LCS regions, but they cannot affect the set and reset jumps happening from LCS to HCS and vice versa, respectively. We constructed earlier (Fig. 4*D*) 1D histograms to extract the set and reset voltages. Another way to statistically analyze the set and reset processes is by constructing a $\frac{\Delta G}{G_0}$ histogram, where $\Delta G = G[i] - G[i-1]$ and $G[i]$ is the zero bias conductance at the end of the ith cycle. A reset (step down) from HCS to LCS has a negative ΔG while a set has a positive ΔG. Fig. 3*C* shows the constructed histogram over all the VEB datasets. The vertical axis is plotted in logarithmic scale for better visualization. The set and reset events correspond to bigger changes in the conductance and thus have larger ΔG values and are present close to zero in the normalized conductance log scale. These are enclosed by blue dashed ovals in Fig. 3*C*. The small fluctuations in the HCS and LCS plateaus will form groups that will sit far away from the center with higher negative values. These are enclosed by black dashed ovals. We can resolve here the set and reset jump events in the complete statistical dataset, giving an alternate univocal confirmation of resistive switching. In Fig. 3 *D* and *E* we plot the separate 2D histograms for only the devices that show switching behavior and otherwise. As expected, the set and reset regions are visible only in devices that show switching.

Schottky Barrier Evidence

The formation of Si-nanocrystalline pathways between the two graphene electrodes and their oxidation (to SiO_x) causes resistive switching as shown by He et al. (35, 36). Although we cannot directly verify this with our statistical analysis presented here, we expect that such semiconducting filaments or nanocrystalline pathways should also create Schottky barriers with the graphene on top.

To explore this we searched for a Schottky diode signature in the individual IV traces. The presence of a Schottky barrier should give a kink at the threshold or "knee" voltage (V_{knee}) in the IV trace. See Fig. 5*A* for an example trace with a kink. To extract this we selected first all the positive curvature IV traces. Then we differentiated the current twice with the voltage, which should give a peak at the position of the kink (Fig. 5*B*). To avoid spurious spikes that could appear while differentiating noise in the traces, a Savitzky–Golay filter is used for smoothing. We did this double derivative for each IV trace for all the devices and then binned their sum over different voltage values. Fig. 5*C* shows the generated $d^2\,I/dV^2$ plot that has a strong positive peak with a mean of around 2.3 V. The results shown in Fig. 5 *A* and *B* are for an example trace of a single device. Along with the 2.3-V peak, multiple other kinks and peaks are also visible. We can speculate that multiple factors contribute to this, which include atomic-scale fluctuations and geometrical rearrangements due to the sudden surge (increase) in current as the voltage across the device exceeds the Schottky limit (46, 47).

To confirm whether this peak indeed corresponds to the Schottky diode, we collected all the individual traces that contribute to the peak and plotted an IV histogram (Fig. 5*D*). There is a kink in IVs in the selected statistical ensemble. Usually, Schottky barriers are characterized by calculating the barrier heights; however, such a calculation requires certain preinformation about the semiconductor, like Richardson's constant. Due to lack of such information, we could calculate only the knee voltage (V_{knee}) after which the electrons that are pumped in through the graphene leads have enough energy to go over the Schottky barrier. These traces with Schottky diode characteristics are distributed nearly everywhere on the positive curvature if plotted in the curvature histograms;

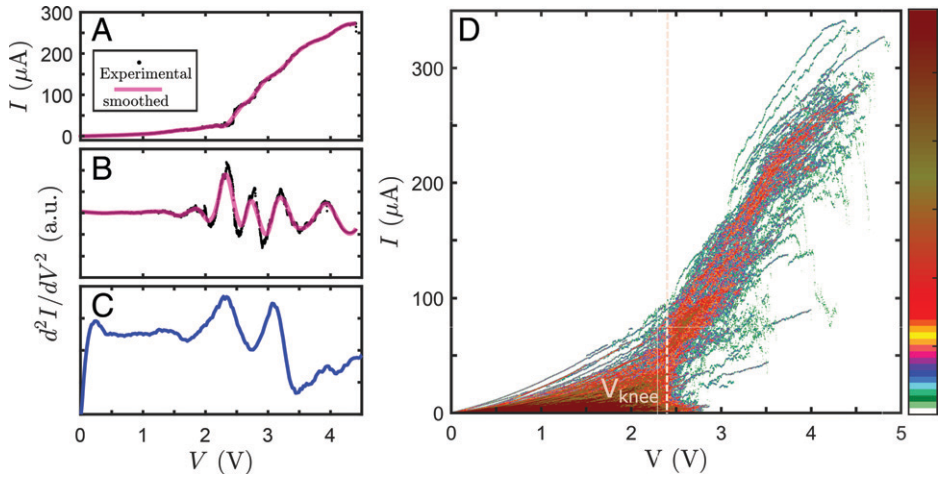

Fig. 5. (*A*) Example IV trace of an individual device showing a kink structure and a corresponding smooth fit. (*B*) The $\frac{d^2I}{dV^2}$ plot for above IV trace showing a peak at the position of the kink. (*C*) Average of all the $\frac{d^2I}{dV^2}$ traces binned along the voltage axis. (*D*) IV trace histograms of vacuum electrobreakdown for graphene on SiO_2 showing a sudden rise in current after a knee voltage (diode characteristics) due to the formation of a Schottky barrier between graphene and the semiconducting filament formed underneath.

however, localization could be spotted near the HCS or ON state (*SI Appendix*, Fig. S10). This provides a further confirmation of why the kinks observed here are not due to Fowler–Nordheim (FN) tunnelling. FN tunnelling is usually attributed to metal–insulator–metal systems or for large tunnel gaps. He et al. (35) also used it to describe their OFF state.

Effect of Substrate

For further investigation, we repeated the VEB also for Al_2O_3, AlN, and quartz substrates using the same feedback control protocol. The EB of graphene over bulk quartz substrate was difficult and, in many instances, the junction did not break even up to 10 V. This is interesting because Candini et al. (30) have shown that it was not possible to do VEB for graphene on SiC, while it works for SiO_2 substrate, suggesting the oxygen content in the substrate is the key to electrobreakdown in vacuum. The quartz crystal has sufficient oxygen content but the EB still does not occur. We attribute this to better heat dissipation through bulk quartz, resulting in less efficient heating of graphene than with the layered substrates. The addition of thin SiN, Al_2O_3, or SiO_2 layers adds additional thermal interface resistances between graphene and the bulk Si heat sink, resulting in a poorer cross-plane heat dissipation, even if the in-plane heat dissipation within the thin layers is high. The VEB of graphene on Al_2O_3 and AlN showed a similar statistical signature to that for SiO_2. All corresponding plots are provided in *SI Appendix*, Figs. S2–S8. We observed here a similar resistive switching and the presence of a Schottky barrier was also recorded. We thus expect a semiconducting filament is also being formed here. It will not be crystalline Si nanoparticles, but something else. We can extract the corresponding V_{knee} voltages for these other substrates and they are also tabulated in Table 2. But it is difficult to say anything about the composition of the filaments using just that. Also, the switching mechanism here could be different from the redox mechanism that exists for SiO_2 substrate. The corresponding d^2 I/dV^2 plots for all the substrates are also provided in *SI Appendix*, Fig. S9.

Table 2. Schottky barrier threshold voltage for the filaments

Substrate	V_{knee}, eV (devices)
SiO_2	2.26(95)
Quartz	2.7(31)
AlN	2.48(28)
Al_2O_3	2.36(38)

Multiple factors could influence the electrical breakdown process in graphene, which include oxygen content in substrate and the environment; the local temperature variations on the graphene (which can depend on the position of defects, localized charge accumulations, etc.); and heat conductance pathways through the substrate, graphene, and the medium or environment. The differences in the conductance histograms for different substrates would depend on all of these. To pinpoint their individual contributions and to study what happens to the substrate (for example, filament formation) would require performing high-resolution TEM imaging or some type of surface nanochemical analysis during the electrobreakdown (29). This would be interesting to see; however, the challenge here is also to do it on a large number of devices to get statistically relevant conclusions.

Conclusion

We have shown how one can perform statistical analysis on the data acquired during feedback-controlled electrobreakdown of graphene. We plotted 2D-conductance histograms for electrobreakdown in different environments and different substrates. This analysis suggests that while electrobreakdown is taking place in air, below a threshold zero-bias conductance (around 0.1 G_0), the graphene effective notch width starts to decrease exponentially. We have demonstrated how the statistical signature of electrobreakdown changes drastically as we decrease the pressure. We studied electrobreakdown on SiO_2, AlN, Al_2O_3, and bulk quartz substrates and observed that electrobreakdown in a vacuum is also closely linked to the chosen substrate and the process behind vacuum electrobreakdown is substrate-mediated sublimation of graphene. This substrate-mediated sublimation further leads to the creation of semiconducting filaments, which forms a Schottky barrier with the graphene on top and also causes resistive switching. These resistive switchings either are activated without electroforming or require very small electroforming voltage that could be due to the small controlled nanogaps creation. We deduced also the threshold voltage of the Schottky barriers for filaments formed over different substrates. Further theoretical and experimental studies would be required to deduce the composition of these filaments in the case of AlN and Al_2O_3 substrate and learn the corresponding resistive switching mechanism.

Our conclusions here are all robust in nature, as the analysis was performed on a large dataset and thus helps us understand the electrobreakdown process as a whole rather than the characteristics derived from individual traces. This could also become a useful tool to understand the transport properties of single molecules deposited on such graphene nanojunctions.

Materials and Methods

Identical bowtie graphene devices are fabricated as wafers as follows: The graphene is grown via chemical vapor deposition (Graphenea S.A.) and transferred onto a prepatterned quartz or doped Si wafer with 300 nm of SiO_2 substrate with Cr/Au electrodes. The graphene is patterned into a 200 nm-wide bowtie-shaped constriction using electron-beam lithography and oxygen plasma etching (16). In some cases before graphene transfer an additional 20-nm layer of Al_2O_3 or AlN is deposited on top of SiO_2 by atomic layer deposition.

Data Availability. Raw data and analysis script have been deposited at the Oxford University Research Archive (48). All other study data are included in this article and/or *SI Appendix*.

ACKNOWLEDGMENTS. C.E., S.T., J.L.S., J.C., X.B., J.T., J.A.M., and G.A.D.B. acknowledge the Quantum Effects in Electronic Nanodevices (QuEEN) Programme Grant EP/N017188/1. J.A.M. was supported through the United Kingdom Research and Innovation Future Leaders Fellowship, Grant MR/S032541/1, with in-kind support from the Royal Academy of Engineering.

1. J. Perrin, *Mouvement Brownien et Réalité Moléculaire* (Masson et Cie, 1909).
2. G. N. Lewis, The atom and the molecule. *J. Am. Chem. Soc.* **38**, 762–785 (1916).
3. A. Aviram, M. A. Ratner, Molecular rectifiers. *Chem. Phys. Lett.* **29**, 277–283 (1974).
4. G. Binnig, H. Rohrer, C. Gerber, E. Weibel, Surface studies by scanning tunneling microscopy. *Phys. Rev. Lett.* **49**, 57–61 (1982).
5. G. Binnig, H. Rohrer, Scanning tunneling microscopy–from birth to adolescence. *Rev. Mod. Phys.* **59**, 615–625 (1987).
6. D. M. Eigler, E. K. Schweizer, Positioning single atoms with a scanning tunnelling microscope. *Nature* **344**, 524–526 (1990).
7. J. A. Stroscio, D. M. Eigler, Atomic and molecular manipulation with the scanning tunneling microscope. *Science* **254**, 1319–1326 (1991).
8. C. Muller, J. Van Ruitenbeek, L. De Jongh, Experimental observation of the transition from weak link to tunnel junction. *Physica C* **191**, 485–504 (1992).
9. N. Agraït, J. G. Rodrigo, S. Vieira, Conductance steps and quantization in atomic-size contacts. *Phys. Rev. B Condens. Matter* **47**, 12345–12348 (1993).
10. J. M. Krans *et al.*, One-atom point contacts. *Phys. Rev. B Condens. Matter* **48**, 14721–14724 (1993).
11. C. J. Muller, J. M. Krans, T. N. Todorov, M. A. Reed, Quantization effects in the conductance of metallic contacts at room temperature. *Phys. Rev. B Condens. Matter* **53**, 1022–1025 (1996).
12. J. Costa-Krämer, N. García, H. Olin, Conductance quantization histograms of gold nanowires at 4 k. *Phys. Rev. B Condens. Matter* **55**, 12910 (1997).
13. A. Yanson, G. R. Bollinger, H. Van den Brom, N. Agrait, J. Van Ruitenbeek, Formation and manipulation of a metallic wire of single gold atoms. *Nature* **395**, 783–785 (1998).
14. F. Evers, R. Korytár, S. Tewari, J. M. van Ruitenbeek, Advances and challenges in single-molecule electron transport. *Rev. Mod. Phys.* **92**, 035001 (2020).
15. F. Prins *et al.*, Room-temperature gating of molecular junctions using few-layer graphene nanogap electrodes. *Nano Lett.* **11**, 4607–4611 (2011).
16. C. S. Lau, J. A. Mol, J. H. Warner, G. A. D. Briggs, Nanoscale control of graphene electrodes. *Phys. Chem. Chem. Phys.* **16**, 20398–20401 (2014).
17. C. Nef *et al.*, High-yield fabrication of nm-size gaps in monolayer CVD graphene. *Nanoscale* **6**, 7249–7254 (2014).
18. J. Moser, A. Barreiro, A. Bachtold, Current-induced cleaning of graphene. *Appl. Phys. Lett.* **91**, 163513 (2007).
19. X. Jia *et al.*, Controlled formation of sharp zigzag and armchair edges in graphitic nanoribbons. *Science* **323**, 1701–1705 (2009).
20. M. R. Sørensen, M. Brandbyge, K. W. Jacobsen, Mechanical deformation of atomic-scale metallic contacts: Structure and mechanisms. *Phys. Rev. B Condens. Matter Mater. Phys.* **57**, 3283 (1998).
21. N. Agraıt, A. L. Yeyati, J. M. Van Ruitenbeek, Quantum properties of atomic-sized conductors. *Phys. Rep.* **377**, 81–279 (2003).
22. D. van Vreumingen, S. Tewari, F. Verbeek, J. M. van Ruitenbeek, Towards controlled single-molecule manipulation using "real-time" molecular dynamics simulation: A GPU implementation. *Micromachines (Basel)* **9**, 270 (2018).
23. C. Evangeli *et al.*, Experimental evidence of disorder enhanced electron-phonon scattering in graphene devices. *Carbon* **178**, 632–639 (2020).
24. J. G. Simmons, Generalized formula for the electric tunnel effect between similar electrodes separated by a thin insulating film. *J. Appl. Phys.* **34**, 1793–1803 (1963).
25. N. Matthews, M. J. Hagmann, A. Mayer, Comment: "generalized formula for the electric tunnel effect between similar electrodes separated by a thin insulating film" [*J. Appl. Phys.* 34, 1793 (1963)]. *J. Appl. Phys.* **123**, 1793 (2018).
26. A. Barreiro, F. Börrnert, M. H. Rümmeli, B. Büchner, L. M. Vandersypen, Graphene at high bias: Cracking, layer by layer sublimation, and fusing. *Nano Lett.* **12**, 1873–1878 (2012).
27. H. Zhang *et al.*, Visualizing electrical breakdown and ON/OFF states in electrically switchable suspended graphene break junctions. *Nano Lett.* **12**, 1772–1775 (2012).
28. O. Cretu *et al.*, Electrical transport measured in atomic carbon chains. *Nano Lett.* **13**, 3487–3493 (2013).
29. O. Dyck *et al.*, Mapping conductance and switching behavior of graphene devices in situ. *Small Methods* **6**, 2101245 (2021).
30. A. Candini *et al.*, Electroburning of few-layer graphene flakes, epitaxial graphene, and turbostratic graphene discs in air and under vacuum. *Beilstein J. Nanotechnol.* **6**, 711–719 (2015).
31. M. El Abbassi *et al.*, From electroburning to sublimation: Substrate and environmental effects in the electrical breakdown process of monolayer graphene. *Nanoscale* **9**, 17312–17317 (2017).
32. L. Pósa *et al.*, Multiple physical time scales and dead time rule in few-nanometers sized graphene–SiO_x-graphene memristors. *Nano Lett.* **17**, 6783–6789 (2017).
33. Y. F. Chang *et al.*, Understanding the resistive switching characteristics and mechanism in active SiO_x-based resistive switching memory. *J. Appl. Phys.* **112**, 123702 (2012).
34. Y. F. Chang *et al.*, Oxygen-induced bi-modal failure phenomenon in SiO_x-based resistive switching memory. *Appl. Phys. Lett.* **103**, 033521 (2013).
35. C. He *et al.*, Multilevel resistive switching in planar graphene/SiO2 nanogap structures. *ACS Nano* **6**, 4214–4221 (2012).
36. C. He *et al.*, Tunable electroluminescence in planar graphene/SiO(2) memristors. *Adv. Mater.* **25**, 5593–5598 (2013).
37. T. Usui *et al.*, Approaching the limits of dielectric breakdown for SiO2 films deposited by plasma-enhanced atomic layer deposition. *Acta Mater.* **61**, 7660–7670 (2013).
38. C. A. Martin *et al.*, Fullerene-based anchoring groups for molecular electronics. *J. Am. Chem. Soc.* **130**, 13198–13199 (2008).
39. M. T. Gonzalez *et al.*, Break-junction experiments on acetyl-protected conjugated dithiols under different environmental conditions. *J. Phys. Chem. C* **115**, 17973–17978 (2011).
40. W. Gao, P. Xiao, G. Henkelman, K. M. Liechti, R. Huang, Interfacial adhesion between graphene and silicon dioxide by density functional theory with van der Waals corrections. *J. Phys. D Appl. Phys.* **47**, 255301 (2014).
41. M. Y. Han, B. Özyilmaz, Y. Zhang, P. Kim, Energy band-gap engineering of graphene nanoribbons. *Phys. Rev. Lett.* **98**, 206805 (2007).
42. Z. J. Qi *et al.*, Correlating atomic structure and transport in suspended graphene nanoribbons. *Nano Lett.* **14**, 4238–4244 (2014).
43. M. K. Hota, D. H. Nagaraju, M. N. Hedhili, H. N. Alshareef, Electroforming free resistive switching memory in two-dimensional vox nanosheets. *Appl. Phys. Lett.* **107**, 163106 (2015).
44. S. Munjal, N. Khare, Electroforming free controlled bipolar resistive switching in Al/CoFe2O4/FtO device with self-compliance effect. *Appl. Phys. Lett.* **112**, 073502 (2018).
45. P. Pal, Y. H. Wang, Interconversion of complementary resistive switching from graphene oxide based bipolar multilevel resistive switching device. *Appl. Phys. Lett.* **117**, 054101 (2020).
46. L. Pósa *et al.*, Noise diagnostics of graphene interconnects for atomic-scale electronics. *npj 2D Mater. Appl.* **5**, 1–9 (2021).
47. H. Sadeghi *et al.*, Conductance enlargement in picoscale electroburnt graphene nanojunctions. *Proc. Natl. Acad. Sci. U.S.A.* **112**, 2658–2663 (2015).
48. C. Evangeli *et al.*, Data and analysis scripts for: Statistical signature of electroburning in graphene nano-junctions. Oxford University Research Archive. https://doi.org/10.5287/bodleian:O5pMwNVE0. Deposited 10 June 2022.